

Research Paper

Enhanced visible-light photocatalytic activity of Bi_2MoO_6 nanoplates with heterogeneous $\text{Bi}_2\text{MoO}_{6-x}@\text{Bi}_2\text{MoO}_6$ core-shell structure

Jianhui Guo^a, Lei Shi^{a,*}, Jiyin Zhao^a, Yang Wang^b, Kaibin Tang^{a,c}, Wanqun Zhang^c, Changzheng Xie^a, Xueyou Yuan^a

^a Hefei National Laboratory for Physical Sciences at the Microscale, University of Science and Technology of China, Hefei, Anhui 230026, People's Republic of China

^b Instrumental Analysis Center, Hefei University of Technology, Hefei, Anhui 230009, People's Republic of China

^c Department of Chemistry, University of Science and Technology of China, Hefei, Anhui 230026, People's Republic of China

ARTICLE INFO

Keywords:

Bi_2MoO_6 nanoplate
Surface disorder
Oxygen vacancies
Carrier recombination
Absorption of visible light
Photocatalytic activity

ABSTRACT

A series of Bi_2MoO_6 (BMO) nanoplates with a heterogeneous $\text{Bi}_2\text{MoO}_{6-x}@\text{Bi}_2\text{MoO}_6$ core/shell structure were successfully obtained by reduction with CaH_2 at 140 °C and subsequent reoxidation in air under low temperatures (≤ 250 °C). It is found that the oxygen vacancies mainly exist in the core, while the shell is formed by surface disorder layer with few oxygen vacancies, which is almost stoichiometric. The controllable growth of the surface disorder layer can be realized by the reduction and/or reoxidation temperatures. The reoxidized BMO with the surface disorder layer exhibits about five times higher visible-light photocatalytic activity toward phenol degradation and an order of magnitude higher activity toward methylene blue (MB) degradation than those of the unmodified sample. The visible-light absorption is mainly dominated by the oxygen vacancies through the modulation of the band gap structure, which promote the solar light utilization and photogenerated charge carriers. Density functional theory calculation shows that BMO is a direct band gap semiconductor. It is suggested that the surface disorder layer could suppress the direct recombination of photogenerated carriers and improve surface reactivity, and results in the enhancement of the photocatalytic activity. In addition, the existence of the stoichiometric surface disorder can promote the catalyst stability. It is demonstrated that the reduction-reoxidation method applied here is simple, easily control, and beneficial for the design and realization of heterogeneous core-shell nanostructured photocatalysts to improve visible and infrared optical absorption by engineering the surface disorder and the oxygen vacancies inside core of Bi_2MoO_6 nanoplates and the related nanostructured photocatalysts.

1. Introduction

The waste water problem from industries and human societies has become increasingly in recent years [1,2]. As an efficient method for the decomposition or mineralization of organic contaminants, semiconductor photocatalysis technology has attracted much attention due to its low cost, environmental harmlessness, efficient degradation rate, and stability in reaction [3,4]. For practical applications of photocatalysis technology, a perfect photocatalyst is expected, which should have a proper band gap to provide energetic electrons, efficient photogenerated charge separation and migration, and also a large inhibition of the photocorrosion process [5,6]. Moreover, a smaller enough band gap to allow for efficient absorption overlap with the solar spectrum is also necessary for the photocatalyst to effectively utilize the solar energy [7,8]. Up to now, TiO_2 semiconductor is the most investigated and applied photocatalyst. However, the relatively wide

band gap (~3.2 eV for anatase phase or 3.0 eV for rutile phase) limits its photocatalytic applications, because only ultraviolet light fraction in solar light can be absorbed by TiO_2 (lower than 3–5%). Thus, TiO_2 is not an ideal photocatalyst to efficiently utilize sunlight in naturally environmental purification or remediation [9,10]. The exploration of facile, mile, and effective routes for the rational synthesis of visible-light responsive catalysts with superior photocatalytic activity is highly desired.

It is well known that the photocatalytic activity of photocatalysts is strongly dependent on morphology and structure. Therefore, for a practical application in photocatalysis, the fabrication of desired morphologies and textures is important as well as control in crystallinity, surface area, and composition. Nowadays, many efforts have been devoting to developing high efficient visible light harvesting photocatalysts. Oxygen vacancy, the most general defect in oxide semiconductors, provide a new approach to control the charges

* Corresponding author.

E-mail address: shil@ustc.edu.cn (L. Shi).

separation process, and engineer the electronic structure of semiconductors [11]. Introducing oxygen vacancies into the lattice of TiO_2 photocatalysts can modify the electronic properties and enhance the photocatalytic activity of TiO_2 [12,13]. Several studies have reported that the oxygen vacancies have been achieved by doping with metal ions or non-metal or rare earth elements [14,15]. Besides, different from impurity incorporation, self-doping that produces Ti^{3+} species in TiO_2 has also been demonstrated [13]. Through doping, the solar absorption characteristics of TiO_2 have been improved to some extent. However, theoretical and experimental investigations have demonstrated that doping dose not inevitably translate into a higher photocatalytic activity since the impurity or defect states can trap electrons and facilitate non-radiative recombination, which will reduce the photocatalytic performance [16,17]. For example, nitrogen-doped TiO_2 exhibits the greatest optical response to solar radiation [18], but its absorption in the visible and infrared remains insufficient.

On the other hand, to improved visible-light photocatalytic activity, tailoring the surface structure at the nanoscale under varied synthesis conditions has long been employed for endowing them distinctive properties and gaining insights into the surface structure related properties [19]. Chen et al. [20] reported that the black TiO_2 with surface disorder obtained by high-pressure hydrogenation treatment shows remarkably enhanced solar absorption and superior solar-driven photocatalytic activity, which has triggered tremendous interest over the world, since it presented a new approach to enhancing photocatalytic performance. Surface disorder can be observed by high resolution transmission electron microscopy (HRTEM) as an amorphous shell [20,21], although the atomic level structure has not yet been fully investigated. Surface disorder can affect the photocatalytic activities in different ways. In some cases, the disordered lattice can induce mid-gap states below Fermi level, resulting in large blue shift of VB maximum [22], which is beneficial for visible-light absorption. In addition, surface disorder can decrease spatial overlap of photoexcited holes and electrons, resulting in an enhancement of charge separation [23]. In the recent years, the introduction of surface disorder has been extended to BiOCl [24], ZnO [25] and BiFeO_3 [26], which has obviously improved the visible-light photocatalytic activity. However, the function of the surface disorder layer in the photocatalytic activity is still unclear.

As a member of Aurivillius family, Bi_2MoO_6 (BMO) with the layered bismuth oxide family are of special interest due to their dielectric, ion-conductive, luminescent and catalytic properties [27,28]. Recent results revealed that Bi_2MoO_6 may be a potential candidate as an excellent photocatalyst and solar-energy-conversion material for water splitting and degradation of organic compounds under visible-light irradiation [29,30]. However, when illuminated under visible light irradiation, the relatively high recombination rate of photogenerated electrons/holes pairs for pure Bi_2MoO_6 hinders its widely application. Approaches such as doping [31,32] and heterojunction formation [33] have been adopted to suppress the recombination of photogenerated electrons/holes pairs. Moreover, as a highly anisotropic semiconductor oxide with a layered crystal structure, the photocatalytic performance of BMO is very sensitive to the exposed surface [30,34]. In the present study, Bi_2MoO_6 nanoplates with a heterogeneous $\text{Bi}_2\text{MoO}_{6-x}\text{@}\text{Bi}_2\text{MoO}_6$ core-shell structure were controllably synthesized by a simple reduction-reoxidation method using CaH_2 as reductant. Unlike the situation in the black hydrogenated TiO_2 nanocrystals [20] with a crystalline core and highly disordered/doped surface layer, it is found that the oxygen vacancies of BMO are “healed” through subsequent low-temperature ($\leq 250^\circ\text{C}$) reoxidation in the core, while surface disorder layer with few oxygen vacancies is grown, which led to an enhanced photogenerated charge transfer and separation, and visible-light photocatalytic activity. The reoxidized BMO exhibits about five times higher visible-light photocatalytic activity toward phenol degradation and one order of magnitude higher activity toward methylene blue (MB) degradation than those of the unmodified BMO. It is demonstrated that the reduction- reoxidation method applied here is simple, easily

control, and beneficial for the design and realization of heterogeneous core-shell nanostructured photocatalysts to improve visible and infrared optical absorption by engineering the surface disorder and the oxygen vacancies inside core of Bi_2MoO_6 nanoplates.

2. Experimental

2.1. Sample preparation

Bi_2MoO_6 nanoplates were synthesized by co-precipitation method. Materials and reagents, $\text{Bi}(\text{NO}_3)_3\cdot 5\text{H}_2\text{O}$, $\text{Bi}(\text{NO}_3)_3\cdot 5\text{H}_2\text{O}$, HNO_3 , $\text{NH}_3\text{H}_2\text{O}$, CaH_2 were of analytical grade and purchased from Sinopharm Chemical Reagent Co. Ltd. China. 29.1042 g of $\text{Bi}(\text{NO}_3)_3\cdot 5\text{H}_2\text{O}$ and 5.2965 g of $\text{Bi}(\text{NO}_3)_3\cdot 5\text{H}_2\text{O}$ were dissolved in 150 mL of 5 M HNO_3 solution and 150 mL of 5 M $\text{NH}_3\text{H}_2\text{O}$ solution, respectively. Then the $(\text{NH}_4)_6\text{Mo}_7\text{O}_{24}\cdot 4\text{H}_2\text{O}$ solution was slowly added into the $\text{Bi}(\text{NO}_3)_3\cdot 5\text{H}_2\text{O}$ solution with continuously stirring. The pH value was adjusted to about nine using concentrated ammonia. After stirring for 30 min at room temperature, the suspension was dried at 120°C overnight and washed by deionized water to remove NH_4NO_3 . And then, the well-crystallized Bi_2MoO_6 (denoted as BMO-AP) was obtained by heating the resulting powder at 300°C for 5 h.

Reduced Bi_2MoO_6 , denoted as BMO-Rd, was synthesized by reducing BMO-AP with CaH_2 as a reductant. 1 g of BMO-AP was mixed with 1 g of CaH_2 and ground. During the grinding procedure, moderate amount of petroleum ether was added in order to avoid deliquescence of CaH_2 in moist air. After sufficient grinding, the mixture was sealed in an evacuated 20 mL capacity glass tube and heated at 140°C for more than 12 h until it totally turned into black, which is to ensure that oxygen vacancies were homogeneously introduced throughout the entire nanoplate. It is found that the sample did not change its color obviously at 100°C but partly decomposed to metallic Bi at 180°C , indicating that the synthesis of BMO-Rd is sensitive to reducing temperature. Besides, the reduction is also sensitive to the ratio of BMO-AP to CaH_2 , and the loading degree of the glass tube. After reduction, excess CaH_2 and the by-products were washed out with 0.1 M NH_4Cl methanol solution (typically 4×100 mL). And the residue was further washed with pure methanol and dried under vacuum.

To obtain the reoxidized samples, BMO-Rd was divided into several parts, and two of them were annealed at 150°C and 250°C in air for 5 h, respectively, with a heating rate of 1 °C/min. After annealing, the color of the sample turned into pale yellow (at 150°C) or yellow (at 250°C). The reoxidized samples are denoted as BMO-Ro150 and BMO-Ro250 respectively, according to the annealing temperatures.

2.2. Material characterization

Crystallographic phases and purity of the samples were identified using an X-ray diffractometer (XRD, Rigaku TTR III) with $\text{Cu K}\alpha$ ($\lambda = 1.54187\text{\AA}$) radiation. The morphology and microstructure were determined by transmission electron microscopy (TEM, JEOL JEM-2100F) with an accelerating voltage of 200 kV. Photoluminescence spectra of powder samples were conducted on a Raman spectrometer (HORIBA LABRAM HR) excited by a 325 nm He-Cd laser. The UV-vis-NIR diffuse reflectance spectra were obtained using a UV-vis-NIR spectrophotometer (Shimadzu SOLID3700) equipped with an integrating sphere. Magnetic measurements were carried out on a superconducting quantum interference device (SQUID) from Quantum Design. Fourier transform infrared spectra (FTIR) were recorded on a FTIR-7600 spectrometer from Lambda Scientific Pty Ltd, using the KBr pellet method. Surface oxidation states and valence band (VB) were investigated by X-ray photoelectron spectroscopy (XPS, Thermo ESCALAB250Xi). The Brunauer-Emmett-Teller (BET) specific surface areas of the prepared samples were analyzed by nitrogen adsorption/desorption isotherms at liquid nitrogen temperature with an Autosorb-iQ analyzer, Quantachrome Instruments.

2.3. Photodegradation test

To evaluate the photocatalytic activities, degradation of model pollutants (phenol and MB) in an aqueous solution under irradiation was carried out as a model reaction. 100 mg of the sample was suspended into 100 mL of 10 ppm pollutant solution and the suspension was magnetically stirred in darkness for 30 min to reach the adsorption equilibrium before irradiation. A 250 W Xenon lamp with a cutoff filter of 420 nm was used as the light source. Aliquots (4 mL) were retrieved from the suspension at certain time intervals and then the catalyst was removed by centrifugation. The concentration of pollutant solution was determined with a UV-vis spectrophotometer (Shimadzu SOLID3700) by measuring the absorption maximum (269 nm for phenol and 664 nm for MB).

2.4. Electrochemical experiments

The Mott-Schottky (MS) measurement and electrochemical impedance spectroscopy (EIS) measurement were performed on a CHI660E electrochemistry workstation (Shanghai, China) at room temperature. All the experiments were carried out in a standard three-electrode cells containing 0.5 mol/L Na_2SO_4 aqueous solution with a platinum foil and a Ag/AgCl electrode as the counter electrode and the reference electrode, respectively. To prepare working electrodes, ITO glass was ultrasonically cleaned in 1 M NaOH aqueous solution, deionized water and acetone, successively. 10 mg sample was dispersed in 0.5 mL of *N,N*-dimethylformamide (DMF) by sonication to get slurry and spread onto the pretreated ITO glass. After dried in air naturally, the working electrode was further dried at vacuum for 6 h to improve adhesion. The area of the electrodes is about $0.7 \times 0.7 \text{ cm}^2$.

2.5. Band structure calculation

The band structure and the density of states (DOS) of BMO were calculated based on density functional theory (DFT), using the CASTEP module [35] within the plane-wave pseudopotential method. The wave functions of the valence electrons were expanded using a plane wave basis set within a specified cutoff energy of 380 eV. The exchange and correlation interactions were modeled using the generalized gradient approximation (GGA), together with the Perdew–Burke–Ernzerhof (PBE) [36]. The core electrons were replaced by the ultrasoft core potentials [37]. The Brillouin zone was sampled with a Monkhorst-Pack k-point grid [38] of $3 \times 1 \times 3$. Convergence was assumed when the residual forces were smaller than $10^{-2} \text{ eV } \text{\AA}^{-1}$. For Bi, Mo, and O, the valence electrons were taken to be $6s^26p^3$, $4s^24p^65s^14d^5$, and $2s^22p^4$, respectively.

3. Results and discussion

3.1. Structure and morphology

The XRD patterns of the BMO samples are shown in Fig. 1, which reveal that all the XRD patterns can be well indexed to a koechlinite phase with the orthorhombic Bi_2MoO_6 crystal structure (JCPDS No. 84-0787, space group: $Pca2_1$) without any impurity. The space group of the crystal structure was unchanged in the reduction and/or reoxidation processes under appropriate experimental control. Besides, the XRD pattern of an over-reduced sample (reduced with CaH_2 at 180°C) is simultaneously displayed in Fig. 1, which reveals the decomposition of BMO-AP to metallic bismuth, suggesting a tolerance limit existing for the amount of oxygen vacancies and the crystal structure stabilization.

The lattice parameters are obtained by fitting the XRD data through Rietveld Refinement, using the Fullprof package (Fig. S1), which are shown in Fig. 2. It is found that the lattice parameters and the volume of the unit cell decrease after reduction and gradually return toward their respective initial values after subsequent reoxidation, which can be

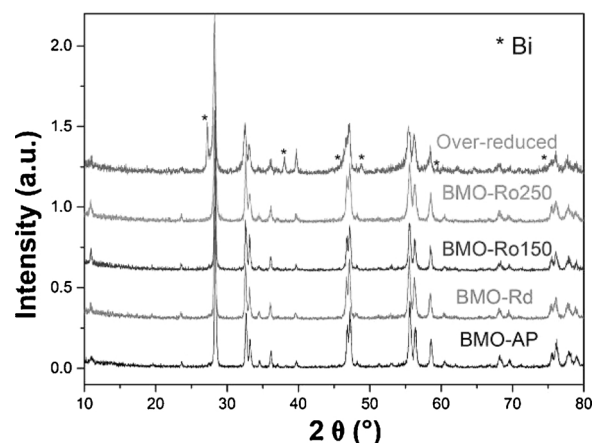


Fig. 1. XRD patterns of BMO-AP, BMO-Rd, BMO-Ro150, BMO-Ro250, and the over-reduced sample.

attributed to the shrinkage of the unit cell induced by the introduction of oxygen vacancies during the reduction, and gradual expansion of the unit cell back toward the initial value due to the refilling of oxygen during reoxidation. These results indicate that the amount of oxygen vacancies can be adjusted by the reduction combining with reoxidation.

The grain sizes and morphologies of the BMO samples are characterized by TEM (Fig. 3). TEM images reveal that all the samples are composed of roughly square-shaped nanoplates with an almost unchanged size ($\sim 20 \text{ nm}$ in thickness and $\sim 200 \text{ nm}$ in side length), indicating that the grains are free from further growth, since the temperatures of subsequent reduction (140°C) and reoxidation ($\leq 250^\circ\text{C}$) are lower than the sintering temperature of the BMO-AP (300°C). The BET specific surface areas analyzed by nitrogen adsorption/desorption isotherms (see Fig. S2) are 7.973, 8.215, 7.233, and $7.027 \text{ m}^2/\text{g}$ for BMO-AP, BMO-Rd, BMO-Ro150, and BMO-Ro250, respectively. Considering the experiment errors, the change of specific surface areas is not apparent, and the size and morphology effects on the optical and photocatalysis properties can be neglected.

3.2. Oxygen vacancies

It is known that the photocatalytic activity is closely related to the oxygen vacancies in BMO. A conventional method to investigate oxygen vacancies in semiconductor photocatalysts is electron paramagnetic resonance (EPR). However, it is found that BMO-Rd does not exhibit obvious EPR signal (see Fig. S3). The absence of EPR signal can confirm but not exclude the existence of oxygen vacancies [39,40]. Here, the magnetic measurements on a SQUID were carried out, which is sensitive enough to detect the weak diamagnetism of a “nonmagnetic” material. As shown in Fig. 4(a), the magnetization versus applied magnetic field loops (M-H) of the samples were recorded at room temperature. The inset of Fig. 4(a) shows the magnetic field dependence of magnetization difference (ΔM), referring to that of the pristine sample. For BMO-AP, a linear M-H curve with a negative slope is found and the magnetic susceptibility is obtained from linear fitting is $-1.775 \times 10^{-6} \text{ emu}/(\text{g Oe})$, which is a typical magnitude for diamagnetism. This is undoubtedly because neither Bi^{3+} ($6s^26p^0$) nor Mo^{6+} ($4d^05s^0$) cations have lone pair electrons. For the remaining samples, the M-H curves are bent and the diamagnetism is suppressed, indicating that Bi^{3+} or Mo^{6+} is partially reduced to Bi^{2+} ($6s^26p^1$) or Mo^{5+} ($4d^15s^0$), respectively. Either of the cases will introduce lone pair electrons and induce weak paramagnetism, and results in the suppression of the diamagnetism. The field dependent ΔM shows a good agreement with the redox procedures, that is, the more oxygen vacancies, the larger ΔM at a certain magnetic field. The results evidently suggest that the oxygen vacancies are gradually reduced with the

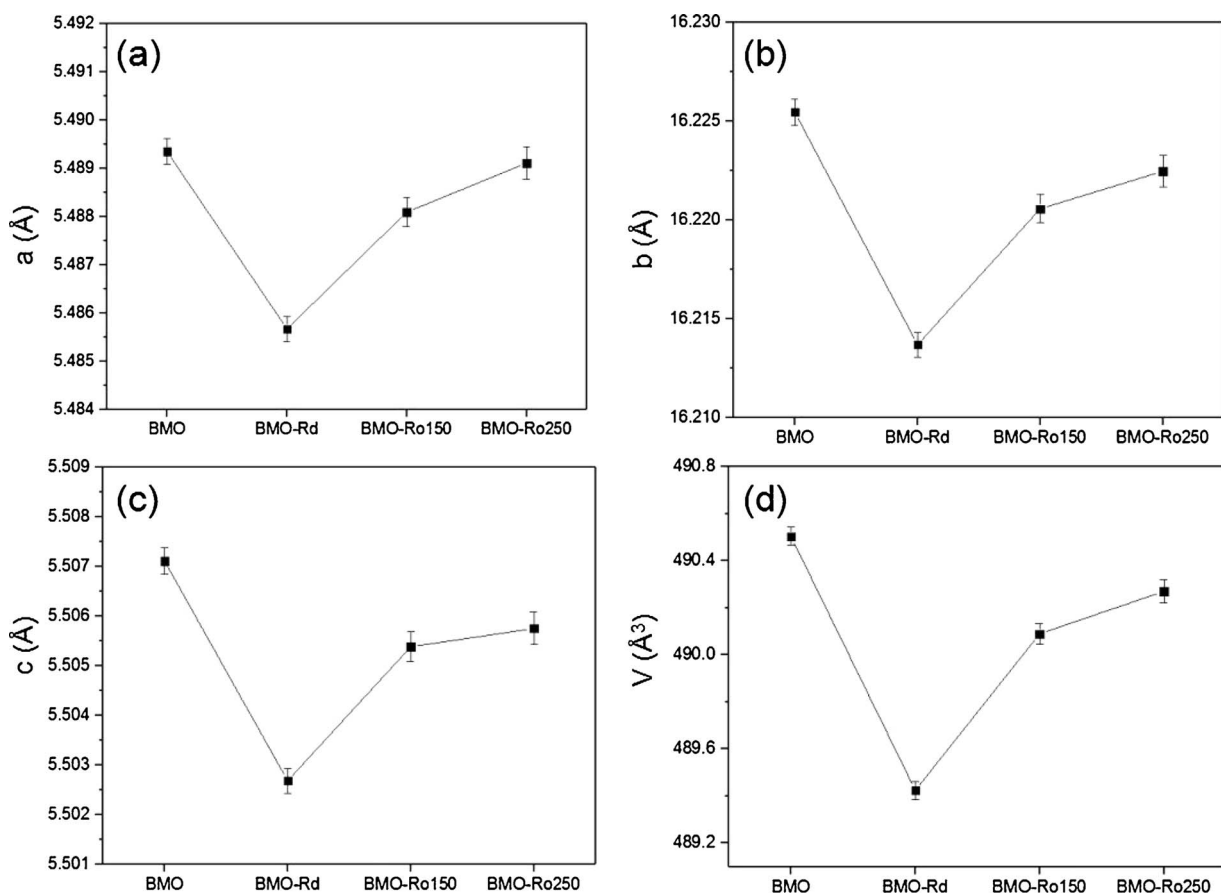


Fig. 2. Refined lattice parameters and unit cell volumes of BMO-AP, BMO-Rd, BMO-Ro150 and BMO-Ro250.

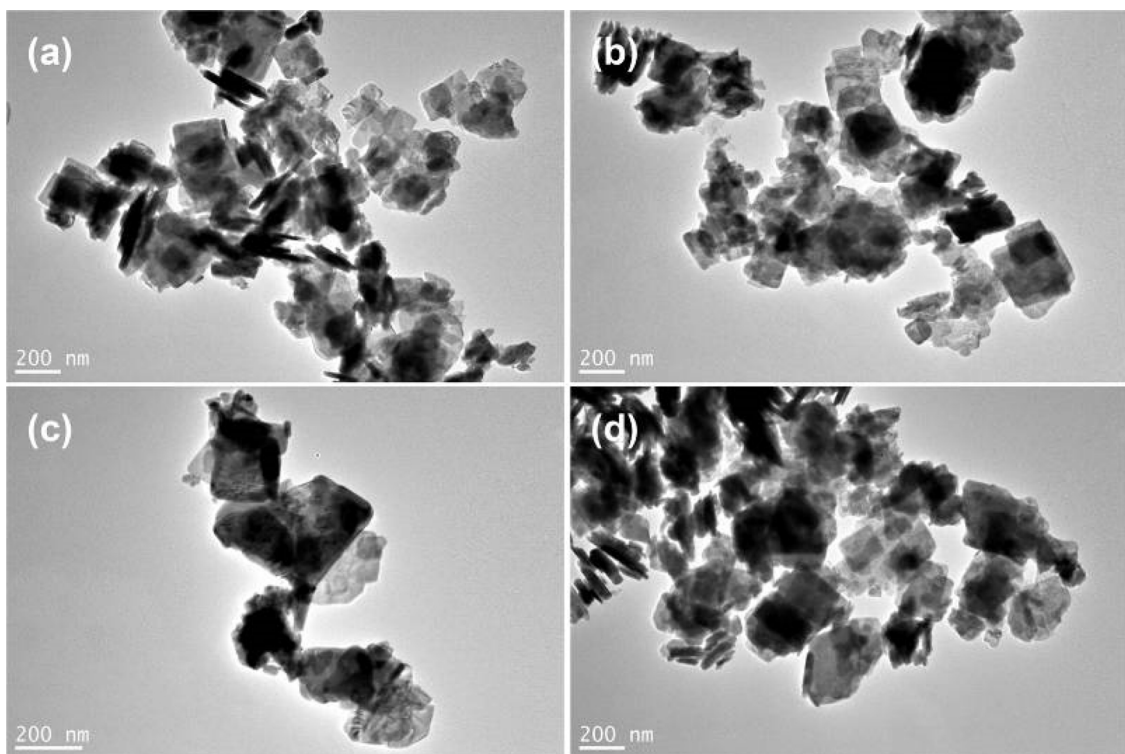


Fig. 3. TEM images of (a) BMO-AP, (b) BMO-Rd, (c) BMO-Ro150, and (d) BMO-Ro250.

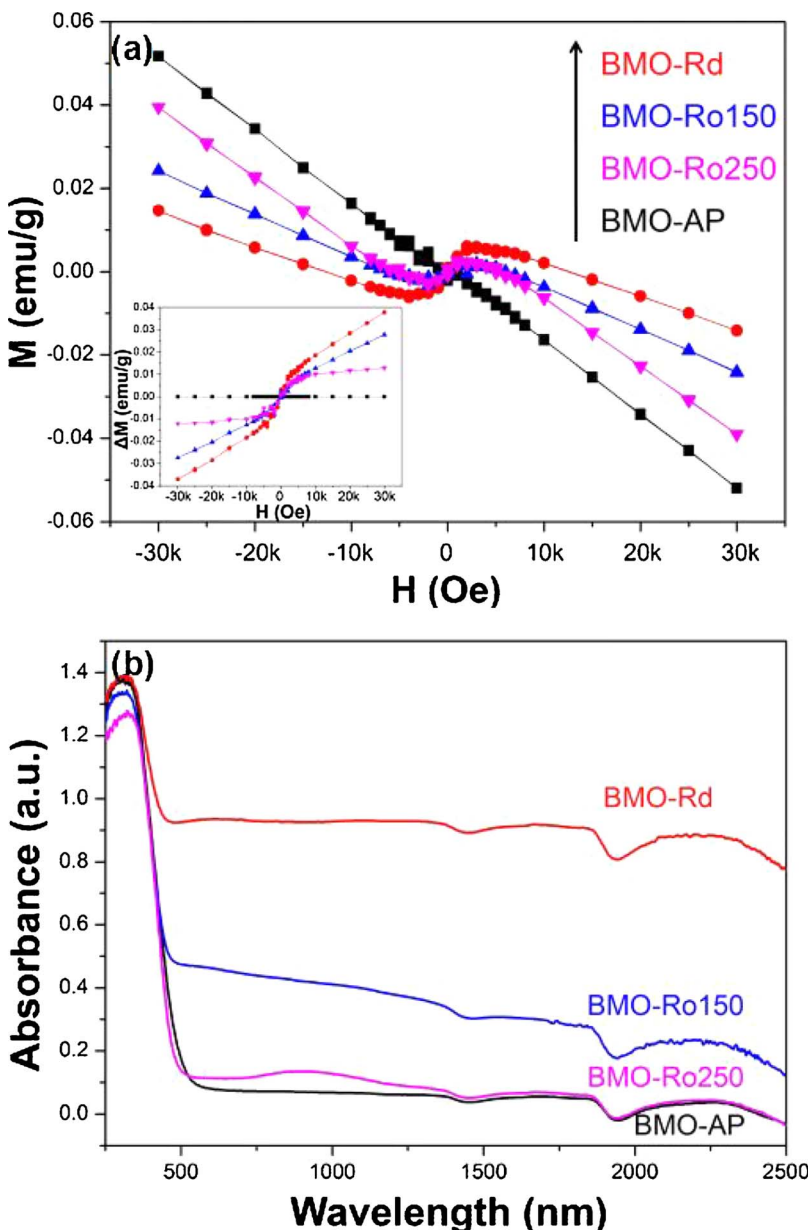


Fig. 4. (a) M-H loops and (b) DRS of BMO-AP, BMO-Rd, BMO-Ro150, and BMO-Ro250 (Inset: ΔM , the differences between the magnetization of BMO-AP and those of the remaining samples).

increase of the reoxidizing temperature.

The solar absorptions of the samples are investigated by diffuse reflectance spectrum (DRS), recorded ranging from 250 to 2500 nm, as shown in Fig. 4(b). In all the DRSs, there is a strong UV absorption, which is induced by electronic transfer from the valence band (VB) to the conduction band (CB) [41]. The most obvious change in the spectra is that the absorbance in the visible and near-infrared ranges remarkably increases after reduction and gradually decreases after reoxidation, which shows a similar trend to that of oxygen vacancies, suggesting that the visible-light absorption is mainly dominated by the oxygen vacancies [42]. The enhancement of visible-light absorption can be attributed to the increase of oxygen vacancies. Meanwhile, the change of sample color corresponding to the visible-light absorption has been seen as shown in Fig. S4. It should be pointed out that compared with that of oxygen vacancies in other reported materials, such as Bi_2MO_6 ($\text{M} = \text{Mo}, \text{W}$) annealing in N_2 [43,44], here the evident function of the oxygen vacancies on the enhanced visible-light absorption is due to the higher amount of oxygen vacancies created by strong CaH_2 reductant. As for the decrease of visible light absorption during reoxidation, it is presumably due to the dilution of bulk defects regarded as

“color centers”, or the decrease of oxygen vacancies, which is caused by the diffusion of oxygen atoms from the air, across the surface, and into the bulk.

The XPS spectra of Bi 4f and Mo 3d levels are shown in Fig. 5, which show an almost unchanged spectrum for all the samples. The oxidation states of Mo and Bi cations are confirmed to be $6+$ and $3+$, respectively, without obvious signal of Mo^{5+} or Bi^{2+} [24,45]. Due to the short probing depth ($\sim \text{nm}$) of XPS, the detected signals mainly reflect the information from the grain surface, which indicates that the grain surface is basically stoichiometric with few oxygen vacancies. Combining with the results of magnetic measurements, it can be concluded that the Bi_2MoO_6 nanoplates (or grains) may be formed by a heterogeneous $\text{Bi}_{2-x}\text{MoO}_6 @ \text{Bi}_2\text{MoO}_6$ core-shell structure, i.e. the oxygen vacancies mainly exist in the core, while the shell is almost stoichiometric, especially for BMO-150 and BMO-250 samples, which is different from the situation of the black hydrogenated TiO_2 nanocrystals where the oxygen vacancies are located in the surface layer [20,21]. This can be understood by reoxidation process that the oxygen diffusion starts from the surface to the bulk. During the reoxidation process, the reoxidation temperature is a crucial factor for the oxygen diffusion. When the

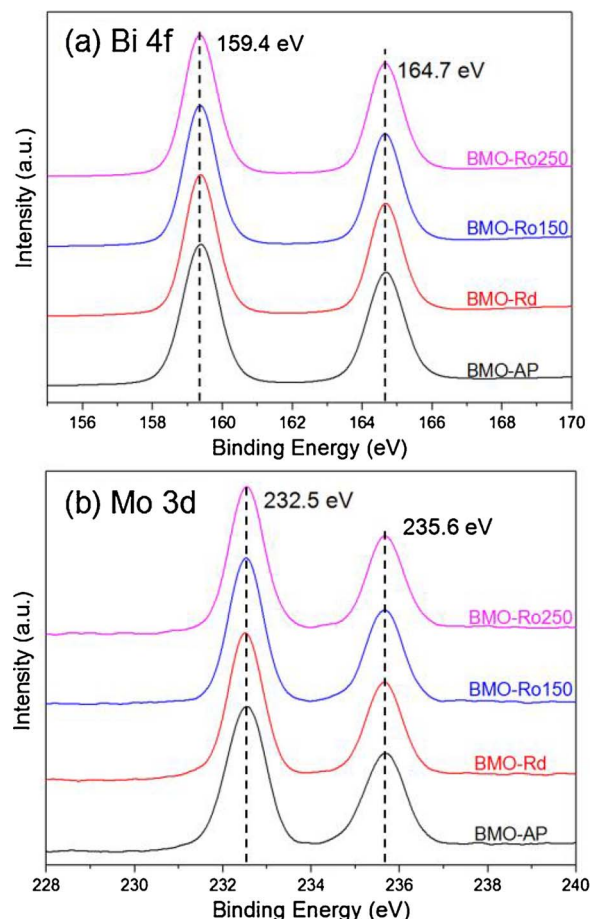


Fig. 5. The XPS spectra of (a) Bi 4f and (b) Mo 3d of BMO-AP, BMO-Rd, BMO-Ro150, BMO-Ro250.

reoxidation temperature is lower, although the speed of atomic diffusion is low, the small amount of oxygen atoms can easily through the surface into the bulk and form an equidistribution. However, when the reoxidation temperature increases, although the speed of atomic diffusion increases, more oxygen atoms will through the surface into the bulk, which may quickly reaction with the surface atoms and form an almost oxygen stoichiometric layer/shell (in fact, it forms a surface disorder layer as observed by high resolution transmission electron microscopy (HRTEM) as shown in following section), and hinders the oxygen diffusion into the core in a limit time. As a result, oxygen vacancies are mainly held in the core, although it has been decreased by oxygen refilling on the oxygen vacancies under the relatively high temperature.

3.3. Surface disorder

To identify the formation and evolution of surface disorder layer during the redox procedures, microstructures of the samples were observed by HRTEM (Fig. 6). Surface disorder layers are found in the edges of nanoplates except in that of BMO-AP. The average thicknesses of the surface disordered layers are about 0.8, 2.5 and 2.2 nm for BMO-Rd, BMO-Ro150, and BMO-Ro250, respectively. These results confirm that the surface disorder layers appear in the reduced Bi_2MoO_6 sample, and grow under the reoxidation temperature of BMO-Rd up to 250 °C.

As a sensitive way to detect the local structure, the measurement of Fourier transform infrared (FTIR) spectrum was carried out to further explore the formation and the evolution of surface disorder. The FTIR spectra of the samples are shown in Fig. 7. An extra sample obtained by reoxidizing BMO-Rd at 400 °C (denoted as BMO-Ro400) is added here to

further confirm the stability of surface disorder at higher temperature. In Fig. 7, the infrared absorption peaks in the range 400–1000 cm^{-1} can be assigned to the typical vibration modes of Bi_2MoO_6 [2,30]. And the absorption bands at about 1634 cm^{-1} and 3443 cm^{-1} are attributed to O–H stretching and deformation vibrations of absorbed water [2]. However, it is found that besides those appear in the spectrum of BMO-AP, two additional peaks at 1415 cm^{-1} and 1473 cm^{-1} appear in spectra of the remaining samples, which are failed to be assigned to any possible impurity phases. Meanwhile, it is found that the intensities of the additional peaks increase at low reoxidation temperature (< 150 °C) and decrease at higher temperatures (> 250 °C). Oxygen vacancies and the related local structure modification are excluded to be the origin of the two additional peaks, since oxygen vacancies are getting fewer during reoxidation, and their related peaks, if existing, would be weakened, which is in contrast to the results of FTIR, suggesting the existence of the surface disorder layer [20,46]. It is worth noting that the trends of peak intensities are consistent with that of the thickness of the surface disorder layer observed by HRTEM (Fig. 6), which indicates that the additional peaks are possibly related to the surface disorder. Moreover, the additional peak intensities evidently decrease for the sample with the reoxidation temperature of ~400 °C, showing that higher reoxidation temperature than the sintering temperature (~300 °C) is disadvantage for the formation of the surface disorder layer. Surface disorder is kinetically stable and the low-temperature method is essential for its formation. It seems that the high mobility of lattice oxygen and the changes in oxygen stoichiometry at a related low temperature, including diffusion of oxygen between the surface and the bulk, play an important role on amorphization of the surface layers [47].

Based on the above results, a diagram illustrating the evolution of surface disorder and oxygen vacancies during redox procedures, the formation of $\text{Bi}_{2-x}\text{MoO}_6@ \text{Bi}_2\text{MoO}_6$ core-shell structure, is drawn in Fig. 8. During the reduction at a temperature as low as 140 °C, surface disorder and oxygen vacancies are created and the sample turns from yellow into black color. Then, during subsequent reoxidation with suitable temperature, oxygen atoms diffuse from the air into the bulk of BMO, refill on the oxygen vacancies, making the color of the sample gradually recovering to the yellow.

3.4. Photocatalytic activity

The visible-light photocatalytic activity was evaluated by monitoring the degradation of phenol, a typical colorless model pollutant, under a 250 W Xenon lamp. The UV absorption spectra of phenol in the range of 230–320 nm were measured to determine its concentration (see Fig. S5). Degradation of phenol dependent on irradiation time is shown in Fig. 9(a), which can be well described by a simplified Langmuir–Hinshelwood model $\ln(C_0/C) = k_a t$, as shown in Fig. 9(b), where C_0 is the initial concentration of dye, C is the concentration of the dye after the irradiation time t , and k_a is the apparent first-order rate constant. The order of degradation rates using different catalysts is as following: BMO-Ro250 > BMO-Ro150 > BMO-Rd > BMO-AP, and the k_a for phenol degradation is enhanced by about 5 times.

The visible-light photocatalytic activity was further evaluated by monitoring degradation of MB, which is selected as a test dye since it has a minimal absorption spectral overlap with that of BMO and a minimal dye sensitization effect, and is more suitable to evaluate the intrinsic visible-light activity of photocatalysts than other dyes [48]. Moreover, MB can be found as a water contaminant from dyeing processes and be a nitrogenous reference compound for evaluating photocatalysts. The UV-vis spectra of MB in the range of 220–800 nm were measured to determine the concentration of MB, as shown in Fig. 10. In general, the discoloration of MB can be attributed to two possible mechanisms, namely the oxidative degradation of MB, and the two-electron reduction to leuco-MB accompanied by the appearance of the absorbance peak at 256 nm [49]. From Fig. 10, however, it is found that

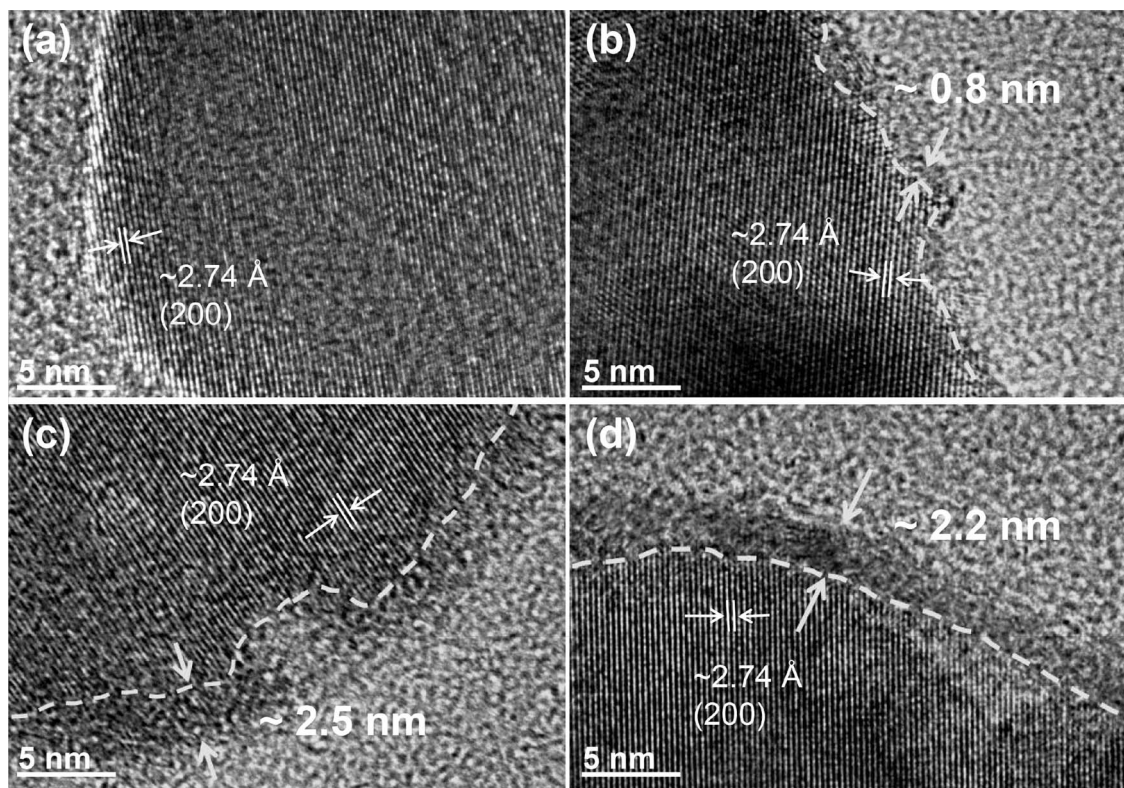


Fig. 6. HRTEM images of (a) BMO-AP, (b) BMO-Rd, (c) BMO-Ro150, and (d) BMO-Ro250.

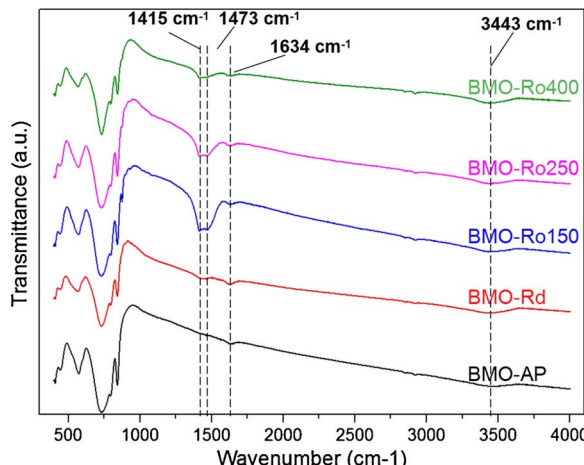


Fig. 7. FTIR spectra of BMO-AP, BMO-Rd, BMO-Ro150, BMO-Ro250, and BMO-Ro400.

there is no signal about the peak at 256 nm in all the degradation tests, indicating that the MB discoloration observed is due to the oxidative degradation.

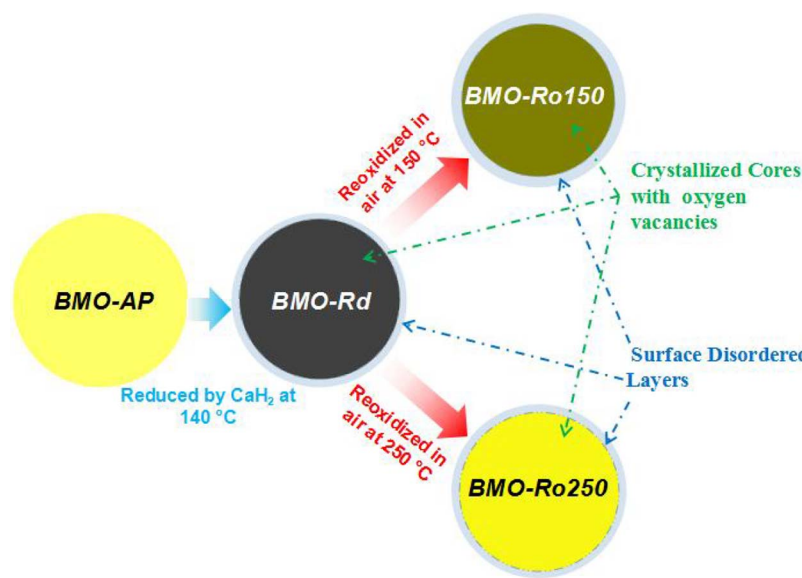
Degradation of MB and $\ln(C_0/C)$ dependent on irradiation time is shown in Fig. 11(a) and (b), respectively. The order of degradation rates using different catalysts is as following: BMO-Ro250 > BMO-Ro150 > BMO-Rd > BMO-AP, which is consistent with the order of the degradation rates of phenol. From Fig. 11(b), it can be obtained that the k_a for MB degradation is enhanced by up to an order of magnitude. These results demonstrate that the reoxidized BMO exhibit a significantly enhanced photocatalytic performance.

It is well known that the photogenerated holes (h^+), superoxide radicals (O_2^-) and hydroxyl radicals ($\cdot OH$) are possible species for photocatalytic oxidation (PCO). In order to understand the underlying mechanism for the PCO reaction of MB over the photocatalysts, we carried out a series of trapping experiments of different active species

for BMO-Ro250. As shown in Fig. 12, when the trapping agent of benzoquinone (BQ, 1 mM), scavenger for O_2^- , was added to the reaction system, compared with the original experiments without radical scavengers, there was only a little change on the degradation of MB, indicating that O_2^- is not the main active species. When *tert*-butyl alcohol (TBA, 1 mM), scavenger for $\cdot OH$, was added, there is a moderate decrease of the degradation rate of MB. When sodium oxalate ($Na_2C_2O_4$, 1 mM), scavenger for h^+ , was added, the degradation is significantly inhibited. These results indicate that h^+ is the main active species for the degradation of MB, and the $\cdot OH$ radicals play a secondary role. In addition, the generation of $\cdot OH$ radicals is confirmed by the $\cdot OH$ -trapping fluorescence spectra (see Fig. S6).

3.5. Mechanism for enhanced photocatalytic activity

In order to investigate the mechanism for enhanced photocatalytic activity, the determination of the position of the conduction band minima (CBM) and valence band maxima (VBM) is important. Here, Mott-Schottky analysis is carried out, as shown in Fig. 13. The calculated flat band potentials of BMO-AP, BMO-Rd, BMO-Ro150, and BMO-Ro250 are -0.51 , -0.42 , -0.44 , and -0.47 eV vs. Ag/AgCl, i.e., -0.31 , -0.22 , -0.24 , and -0.27 eV vs. NHE, respectively. As an n-type semiconductor, the flat band potential is close to the CBM. Therefore, the positions of CBM, E_{CB} , are estimated to be -0.31 , -0.22 , -0.24 , and -0.27 eV vs. NHE for BMO-AP, BMO-Rd, BMO-Ro150, and BMO-Ro250, respectively. The E_{CB} of BMO-AP (-0.31 V vs. NHE) is less negative than the O_2/O_2^- potential (-0.33 V vs. NHE) [50,51]. Moreover, after introduction of oxygen vacancies, the E_{CB} is even less negative (-0.22 V vs. NHE for BMO-Rd), which may be due to the oxygen vacancies acting as n-type dopants and the induced defect levels locating below the CBM [44,52]. Since the E_{CB} is less negative than the O_2/O_2^- potential, the photogenerated electrons are unlikely to react with O_2 to produce O_2^- , which is good agreement with the radical-scavenging MB degradation (Fig. 12). To determine the change of band gap, plots of $(\alpha h\nu)^2$ vs. $h\nu$, base on UV-vis spectra (Fig. 4b),



are plotted in Fig. 13(b). For a crystalline semiconductor, the optical absorption near the band edge follows the equation $a\hbar\nu = A(\hbar\nu - E_g)^{n/2}$, where a , ν , E_g , and A are absorption coefficient, light frequency, band gap, and a constant, respectively [53]. The value of n is determined by the type of transition, for BMO, $n = 1$. The E_g could be thus estimated to be 2.79, 2.69, 2.73, and 2.76 eV for BMO-AP, BMO-Rd, BMO-Ro150, and BMO-Ro250, respectively. It is found that since the introduction of oxygen vacancies will generate inter-gap defect states, the band gap is narrowed, which can improve utilization of visible light and facilitate the generation of holes and electron. Besides, the position of VBM, E_{VB} , can be determined following the equation: $E_{VB} = E_{CB} + E_g$, which are 2.48, 2.47, 2.49, and 2.49 eV for BMO-AP, BMO-Rd, BMO-Ro150, and BMO-Ro250, respectively. The E_{VB} value is more positive than the $\cdot\text{OH}/\text{OH}^-$ potential (1.99 eV vs. NHE) [50,54]. Therefore, the photogenerated holes are able to react with OH^- to produce $\cdot\text{OH}$ radicals for photodegradation of pollutants. The h^+ located at VBM (~ 2.48 eV) could also directly participate in the photocatalytic oxidation reaction. The above findings are in well agreement with the results of the active species-scavenging photodegradation (Fig. 12).

To improve photocatalytic activity, the ability of charge transfer is crucial, thus EIS analysis is carried out. The Nyquist plotting of EIS is

Fig. 8. Diagram for the evolution of surface disorder and oxygen vacancies during low-temperature redox procedures.

shown in Fig. 14. It is found that the diameter of the arc radius of BMO-Rd is smaller than that of BMO-AP, indicating a lower resistance, which is due to that the induced oxygen vacancies act as n-type carrier dopants to improve the conductivity. In general, a small resistance is beneficial to charge transfer, which will enhance the utilization of photogenerated holes and electrons, and improve the photocatalytic activity.

Besides the effects of oxygen vacancies, the effects of surface disorder are also important. As mentioned above, during the reduction and reoxidation, heterogeneous $\text{Bi}_2\text{MoO}_{6-x}@\text{Bi}_2\text{MoO}_6$ core-shell structures are formed, where the oxygen vacancies mainly exist in the core, while the shell is almost stoichiometric with few oxygen vacancies. The enhanced visible-light absorption is mainly dominated by the oxygen vacancies, since they can modulate the band gap structure, and promote the solar light utilization and photogenerated charge carriers [14,26]. However, bulk oxygen vacancies (oxygen vacancies in core) also tend to act as recombination centers of charge carriers [55], which is disadvantageous for the improved photocatalytic performance. In fact, although BMO-Rd with the highest content of oxygen vacancies shows the strongest visible-light absorption, its photocatalytic activity is lower than those of BMO-Ro150 and BMO-Ro250 with gradually decrease of oxygen vacancies (Figs. 9 and 11), again suggesting that the enhanced

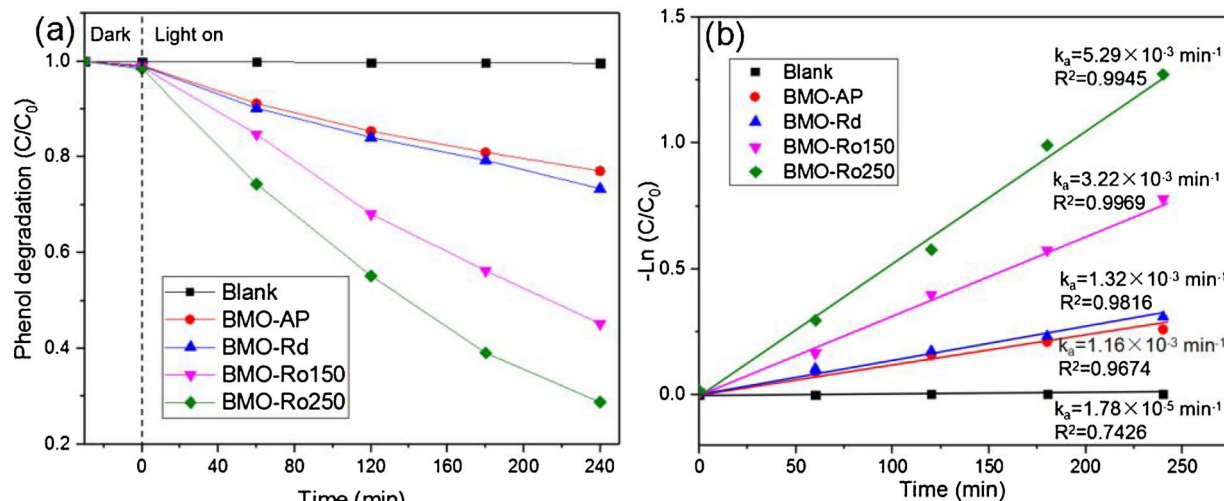


Fig. 9. (a) Degradation of phenol over BMO-AP, BMO-Rd, BMO-Ro150, and BMO-Ro250 in an aqueous solution under irradiation of a 250 W Xenon lamp with a cutoff filter of 420 nm. (b) $\ln(C_0/C)$ of phenol degradation.

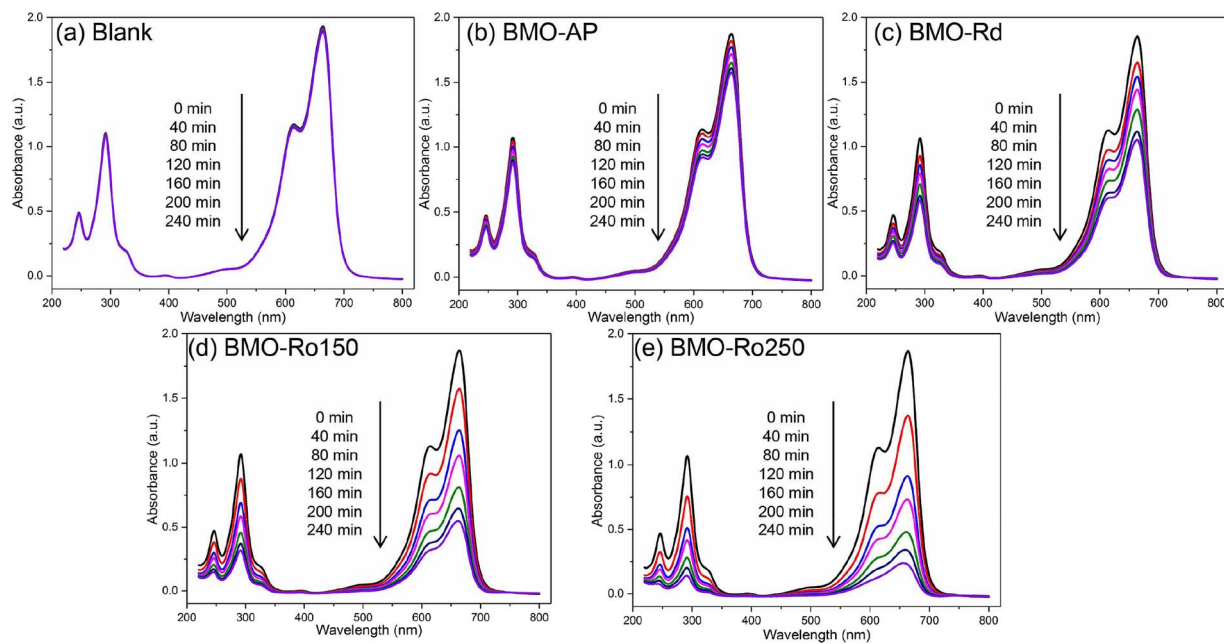


Fig. 10. Degradation of MB (a) without catalyst, and over (b) BMO-AP, (c) BMO-Rd, (d) BMO-Ro150, and (e) BMO-Ro250 in an aqueous solution under irradiation of a 250 W Xenon lamp with a cutoff filter of 420 nm.

visible-light photocatalytic activity can not be solely attributed to the enhanced visible-light absorption by inducing oxygen vacancies in bulk. The effects of surface disordered layer (shell) on the photocatalytic properties should be considered. It has been suggested that local structure modifications of the surface, including the distorted Mo-O and Bi-O polyhedral, play crucial roles in creating surface active sites for trapping molecular H₂O and O₂, as well as for producing active radicals [30,34], which can improve the utilization of the photogenerated charge carriers. As an electron acceptor, the introduction of reduced graphene oxide can make the photogenerated electrons rapidly transferring to the surface instead of jumping back to the valence band and combining with positive holes, therefore improves the photocatalytic activity [56,57]. In this work, the order of photocatalytic activities is as follows: BMO-Ro250 > BMO-Ro150 > BMO-Rd > BMO-AP, which shows the close connection with the growth of the surface disorder layer (Fig. 6). The introduction of surface disorder is an effective way to modify the local structures, resulting in lattice distortions and inhomogeneous ionic distribution on the surface, which is beneficial for the selected acceptance and spatial separation of photoexcited electrons

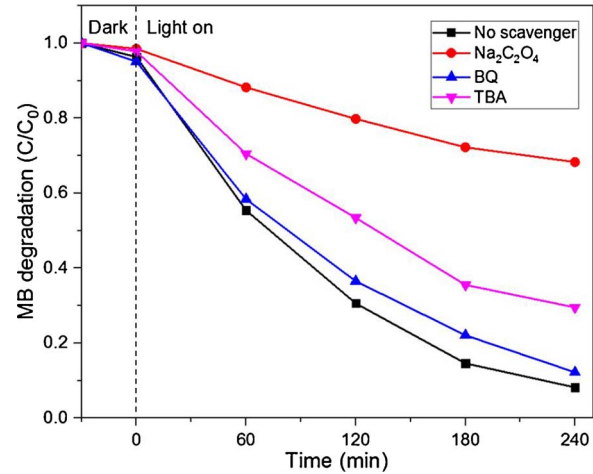


Fig. 12. Photocatalytic degradation of MB under visible-light irradiation with addition of different scavengers using BMO-Ro250 photocatalyst.

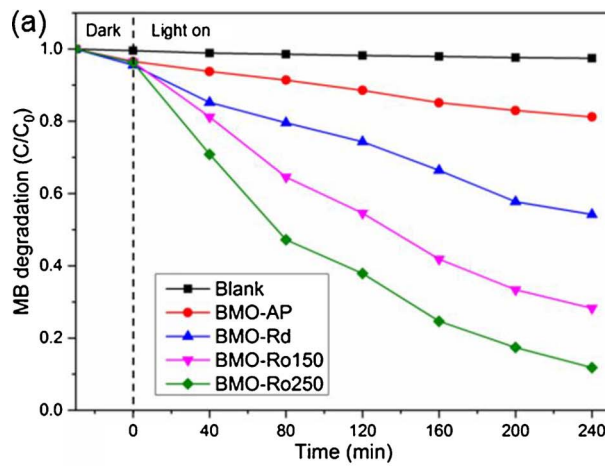


Fig. 11. (a) Degradation of MB over BMO-AP, BMO-Rd, BMO-Ro150, and BMO-Ro250 in an aqueous solution under irradiation of a 250 W Xenon lamp with a cutoff filter of 420 nm. (b) $-\ln(C/C_0)$ of MB degradation.

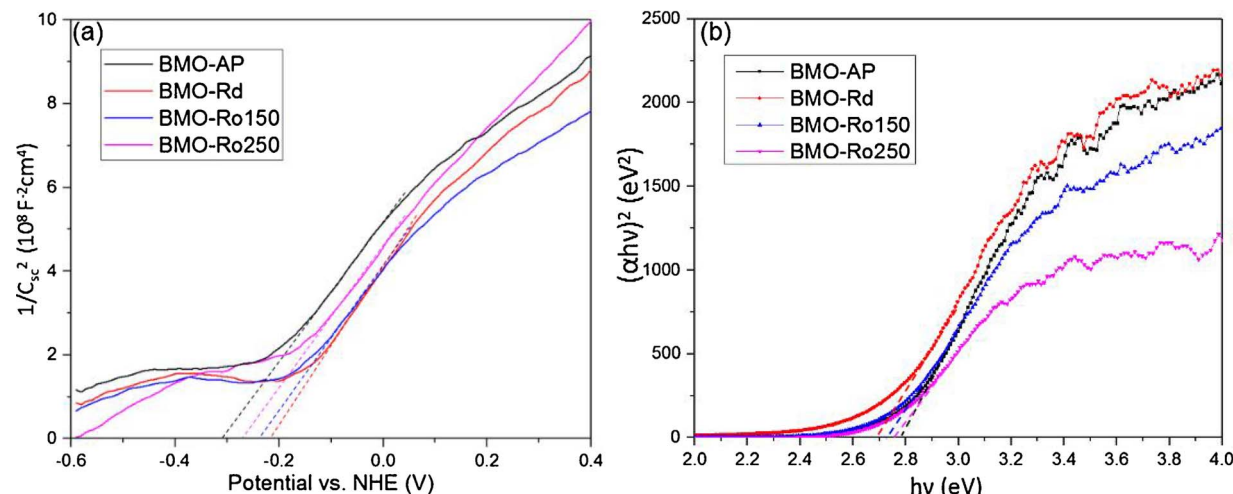


Fig. 13. (a) Mott-Schottky plots of the four BMO samples on an ITO substrate at pH = 7, (b) plots of the $(\alpha h\nu)^2$ vs. the light energy for the BMO samples.

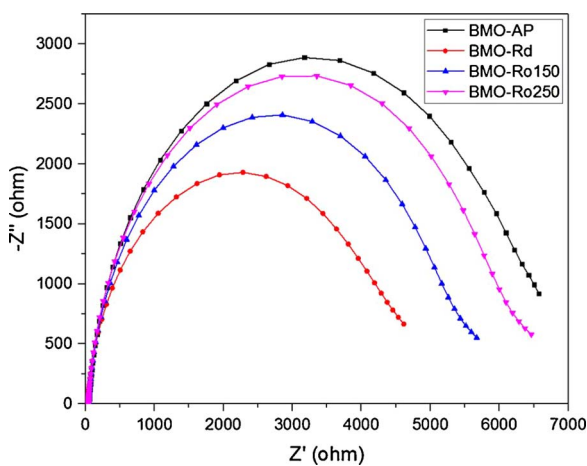


Fig. 14. The Nyquist plots of EIS for the BMO samples.

and holes, as well as the enhancement of surface reactivity. It should be pointed out that all the surface modified samples, even the BMO-Rd with the highest concentration of bulk oxygen vacancies, exhibits higher photocatalytic activity than that of the pristine sample without defects, which just reveals the benefits from surface disorder (from HRTEM image of BMO-Rd, it can be found there is a thin surface disorder layer of around 0.8 nm, which may be induced by the sample exposed in air).

In order to confirm the effect of surface disorder,

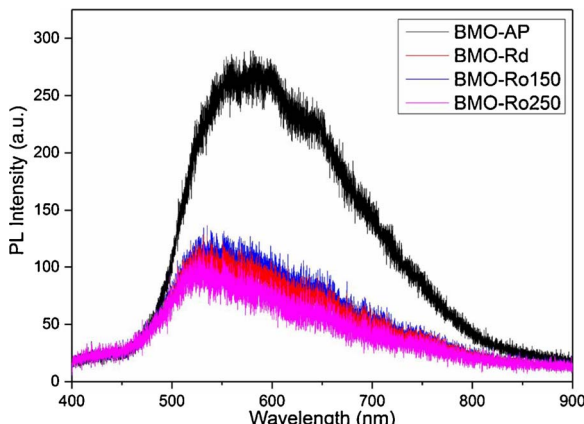


Fig. 15. PL spectra of the BMO samples under excitation at 325 nm.

photoluminescence spectra (PL) were recorded under the excitation of a 325 nm He-Cd laser, as shown in Fig. 15. It is known that the photoluminescence is resulted from the recombination of photogenerated electron-hole pairs [58], which is widely used to evaluate the recombination rate of charge carriers [59]. In Fig. 15, a broad emission peak appears in the range of 450–800 nm. It is found that the PL peak intensities of the three modified samples, namely BMO-Rd, BMO-Ro150, and BMO-Ro250, are obviously lower than that of the pristine sample BMO-AP, indicating a suppression of carrier recombination,

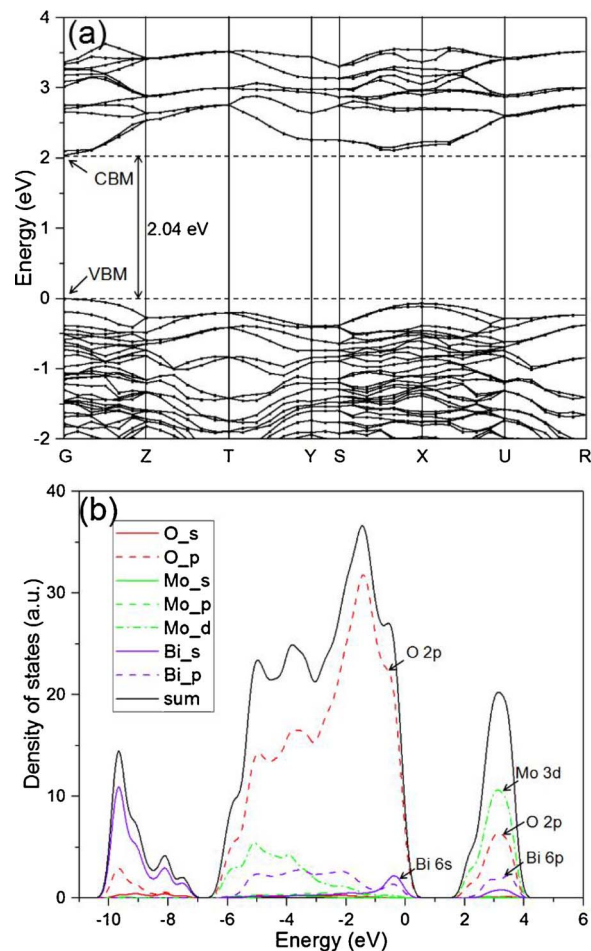


Fig. 16. (a) Band structure and (b) density of states of Bi_2MoO_6 .

which is beneficial for photocatalysis.

To further understand the recombination of the photogenerated electron-hole pairs, the electronic structure of Bi_2MoO_6 was investigated, as shown in Fig. 16(a). From Fig. 16(a), it can be found that both the VBM and the CBM are located near the G point, showing that BMO is a direct band gap semiconductor, which is consistent with previous studies [60,61]. DOS calculation (Fig. 16(b)) shows that the VBM is mainly consist of the O 2p orbital and the CBM is mainly consist of the hybridization of Mo 4d, O 2p and Bi 6p orbitals. As a direct band gap semiconductor, the recombination of charge carriers is fast which is because the electrons located at the CBM and the holes located at the VBM share the same k-vector near the G symmetry point, and the recombination can be achieved through direct transition without assistance of phonons [62].

For a disordered system, the inversion symmetry of the lattice is broken and no well-defined crystal structure can be established. When the inversion symmetry of a direct band gap semiconductor is broken, the photogenerated carriers at the band extrema will locate at different points in k-space, and the direct recombination, which preserves k, will be limited as an indirect band gap semiconductor [63,64]. This result is consistent with the suppressed PL intensity in the experimental results (Fig. 15). Thus, the enhanced photocatalytic activity of BMO-Ro250 can be ascribed to the suppressed recombination of charge carriers owing to surface disorder layer. Based on the above results, possible mechanisms for the improved performance are proposed and schematically illustrated in Fig. 17. Under visible-light irradiation, the $\text{Bi}_2\text{MoO}_{6-x}@\text{Bi}_2\text{MoO}_6$ catalyst is excited to generate electrons and holes at CB and VB, respectively. The oxygen vacancies in the core can provide defect states below CB and narrow the band gap, thus improved the utilization of visible light. The oxygen vacancies also act as carrier dopants and enhance conductivity for charge transfer. At the same time, the shell with distorted lattice (surface disorder) can trap the small molecules and ions such as O_2 , H_2O and OH^- . The surface disorder can also break the inversion symmetry of the crystal lattice and suppressed the direct recombination of the photogenerated charge carriers. After the charge carriers migrate to the surface, the holes can react with OH^- to produce $\cdot\text{OH}$ radicals. Both the holes and $\cdot\text{OH}$ radicals participate in photocatalytic oxidation reaction and the pollutant is then degraded.

3.6. Catalyst stability

The stability of BMO-Ro250 is examined by photodegradation of MB under visible light for five consecutive runs, as shown in Fig. 18. After five cycles, there is only a slight decrease (about 4.49%) on the degradation rate of MB, which may be due to the loss of catalyst in the cycle experiment. After five cycles, the XRD patterns (Fig. 19(a)) show that there is no obvious change on the structure of the sample and the HRTEM image (Fig. 19(b)) shows that the average thickness of the surface disordered layers is still retained about 2.2 nm for BMO-Ro250.

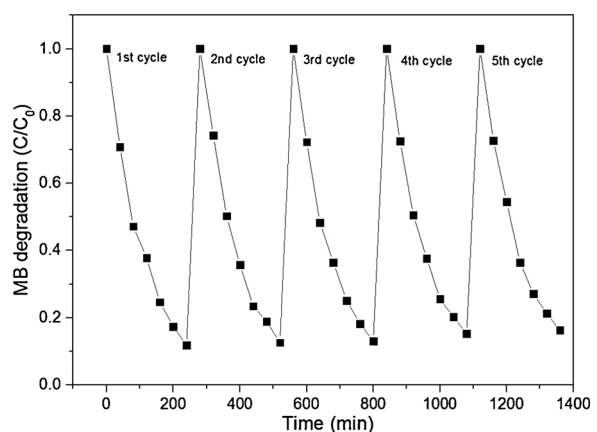


Fig. 18. Cyclic degradation of MB over BMO-Ro250 for five runs.

The sample exhibits well stability and has potential for practical applications.

4. Conclusions

In summary, heterogeneous $\text{Bi}_2\text{MoO}_{6-x}@\text{Bi}_2\text{MoO}_6$ core/shell structure is successfully prepared after reduction by CaH_2 at a temperature as low as 140 °C and subsequent reoxidation at a temperature of up to 250 °C with almost stoichiometric surface-disorder layer and oxygen vacancies in core. The formation of stoichiometric surface disorder is confirmed by HRTEM, FTIR, and XPS. The bulk oxygen vacancies of the reduced BMO can be decreased at an ultra-low reoxidation temperature (< 250 °C), thus the surface disorder can still exist after reoxidation. It is found that the reoxidized sample exhibit remarkably improved photocatalytic activity on degradation of phenol and MB. Density functional theory calculation shows that BMO is a direct band gap semiconductor. The visible-light absorption is mainly dominated by the oxygen vacancies through the modulation of the band gap structure, which promote the solar light utilization and photogenerated charge carriers. It is suggested that the surface disorder layer could suppress the recombination of photogenerated carriers and enhance surface reactivity, and thus results in the enhancement of the photocatalytic activity. In addition, the existence of the stoichiometric surface disorder can promote the catalyst stability. It is demonstrated that the reduction-reoxidation method applied here is simple, easily control, and beneficial for the design and realization of heterogeneous core-shell nanostructured photocatalysts to improve visible and infrared optical absorption by engineering the surface disorder and the oxygen vacancies inside core of Bi_2MoO_6 nanoplates and the related nanosstructured photocatalysts.

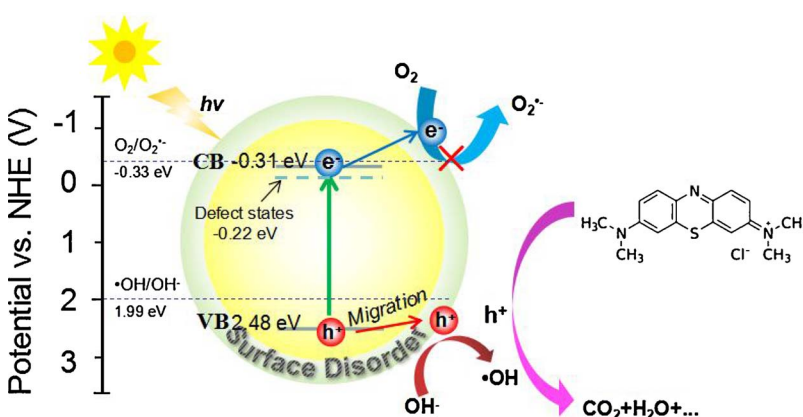


Fig. 17. Schematic illustration of photodegradation over $\text{Bi}_2\text{MoO}_{6-x}@\text{Bi}_2\text{MoO}_6$ under visible light irradiation.

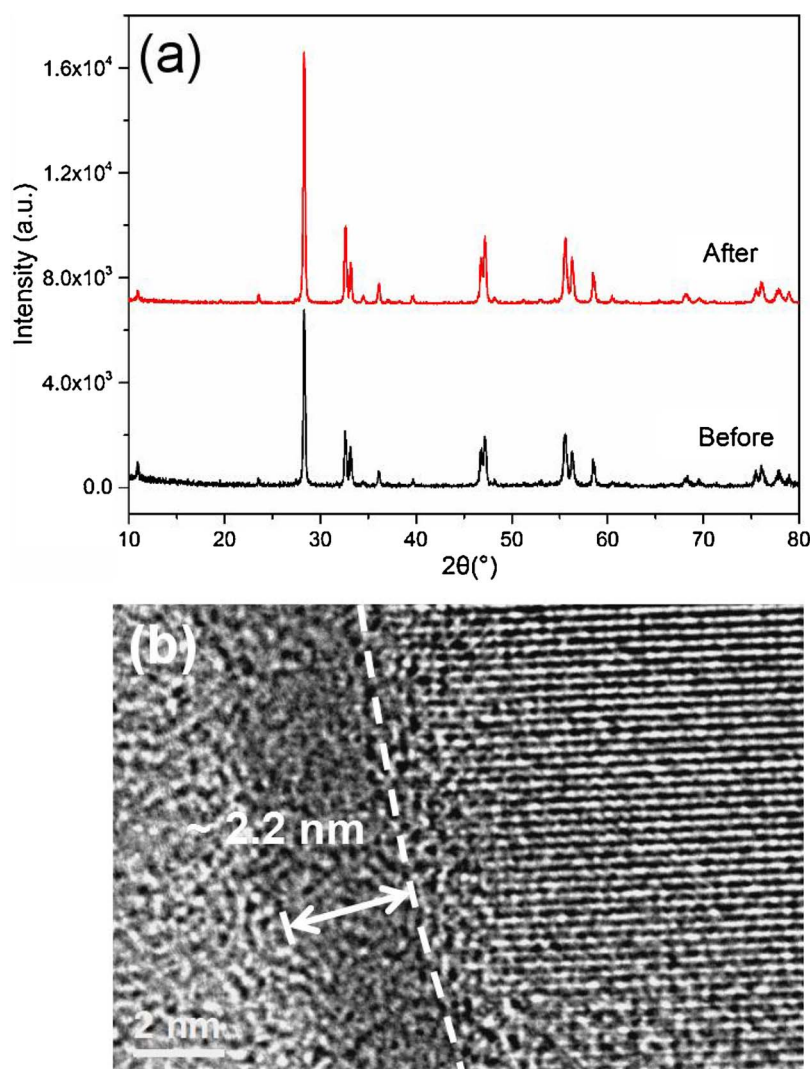


Fig. 19. (a) XRD patterns of BMO-Ro250 before and after photocatalytic reaction for five cycles. (b) HRTEM image of BMO-Ro250 after five reaction cycles.

Acknowledgements

This project was financially supported by the National Natural Science Foundation of China (Grant No. 10874161), and the National Basic Research Program of China (973 Program, Grant No. 2009CB939901). The authors acknowledge Dr. Yan Wang and Dr. Hai Zhu for technical assistance on photodegradation tests, and the Supercomputing Center at USTC for providing the computing resources.

Appendix A. Supplementary data

Supplementary data associated with this article can be found, in the online version, at <http://dx.doi.org/10.1016/j.apcatb.2017.11.030>.

References

- [1] M. Imani, M. Farajnezhad, A. Tadjarodi, Mater. Res. Bull. 87 (2017) 92–101.
- [2] F. Chen, C. Niu, Q. Yang, X. Li, G. Zeng, Ceram. Int. 42 (2016) 2515–2525.
- [3] A. Fujishshima, K. Honda, Nature 238 (1972) 37–38.
- [4] G.M. Wang, Y.C. Ling, Y. Li, Nanoscale 4 (2012) 6682–6691.
- [5] W. Li, Y.H. Deng, Z.X. Wu, X.F. Qian, J.P. Yang, Y. Wang, D. Gu, F. Zhang, B. Tu, D.Y. Zhao, J. Am. Chem. Soc. 133 (2011) 15830–15833.
- [6] Y.H. Ng, A. Iwase, N.J. Bell, A. Kudo, R. Amal, Catal. Today 164 (2011) 353–357.
- [7] G. Tian, Y. Chen, X. Meng, J. Zhou, W. Zhou, K. Pan, C. Tian, Z. Ren, H. Fu, ChemPlusChem 78 (2013) 117–123.
- [8] X. Bai, L. Wang, Y. Zhu, ACS Catal. 2 (2012) 2769–2778.
- [9] S. In, A. Orlov, R. Berg, F. García, S. Pedrosa-Jimenez, M.S. Tikhov, D.S. Wright, R.M. Lambert, J. Am. Chem. Soc. 129 (2007) 13790–13791.
- [10] C.L. Yu, L.F. Wei, J.C. Chen, Y. Xie, W.Q. Zhou, Q.Z. Fan, Ind. Eng. Chem. Res. 53 (2014) 5759–5766.
- [11] W. Bi, C. Ye, C. Xiao, W. Tong, X. Zhang, W. Shao, Y. Xie, Small 10 (2014) 2820–2825.
- [12] D. Ulrike, Surf. Sci. Rep. 48 (2003) 53–229.
- [13] Z. Fan, L. Wang, T. Wu, Z. Zhang, D. Borcharadt, P. Feng, J. Am. Chem. Soc. 132 (2010) 11856–11857.
- [14] H. Li, W. Li, S. Gu, F. Wang, X. Liu, C. Ren, Mol. Catal. 433 (2017) 301–312.
- [15] C. Yu, Z. Wu, R. Liu, D.D. Dionysiou, K. Yang, C. Wang, H. Liu, Appl. Catal. B. Environ. 209 (2017) 1–11.
- [16] R. Asahi, T. Morikawa, T. Ohwaki, K. Aoki, Y. Taga, Science 293 (2001) 269–271.
- [17] T.L. Thompson, J.T. Yates, Chem. Rev. 106 (2006) 4428–4453.
- [18] X. Chen, S.S. Mao, Chem. Rev. 107 (2007) 2891.
- [19] A.T. Bell, Science 299 (2003) 1688–1691.
- [20] X. Chen, L. Liu, P.Y. Yu, S.S. Mao, Science 331 (2011) 746–750.
- [21] A. Naldoni, M. Allietta, S. Santangelo, M. Marelli, F. Fabbri, S. Cappelli, C.L. Bianchi, R. Psaro, V. Dal Santo, J. Am. Chem. Soc. 134 (2012) 7600–7603.
- [22] X. Chen, L. Liu, Z. Liu, M.A. Marcus, W.C. Wang, N.A. Oyler, M.E. Grass, B. Mao, P.A. Glans, P.Y. Yu, J. Guo, S.S. Mao, Sci. Rep. 3 (2013) 1510–1516.
- [23] L. Liu, P.Y. Yu, X. Chen, S.S. Mao, D.Z. Shen, Phys. Rev. Lett. 111 (2013) 065505.
- [24] L. Ye, K. Deng, F. Xu, L. Tian, T. Peng, L. Zan, Phys. Chem. Chem. Phys. 14 (2012) 82–85.
- [25] T. Xia, P. Wallenmeyer, A. Anderson, J. Murowchick, L. Liu, X. Chen, RSC Adv. 4 (2014) 41654–41658.
- [26] S. Wang, D. Chen, F. Niu, N. Zhang, L. Qin, Y. Huang, J. Alloys Compd. 688 (2016) 399–406.
- [27] N. Baux, R.N. Vannier, G. Mairesse, G. Nowogrocki, Solid State Ionics 91 (1996) 243.
- [28] M.S. Islam, S. Lazare, R.N. Vannier, G. Nowogrocki, G.J. Mairesse, Mater. Chem. 8 (1998) 655.
- [29] J.H. Bi, L. Wu, J. Li, Z.H. Li, X.X. Wang, X.Z. Fu, Acta Mater. 55 (2007) 4699.
- [30] L. Zhang, T. Xu, X. Zhao, Y. Zhu, Appl. Catal. B: Environ. 98 (2010) 138–146.
- [31] X. Zhao, J. Qu, H. Liu, Z. Qiang, R. Liu, C. Hu, Appl. Catal. B: Environ. 91 (2009)

- 539–545.
- [32] B. Yuan, C. Wang, Y. Qi, X. Song, K. Mu, P. Guo, L. Meng, H. Xi, *Colloids Surf. A* 425 (2013) 99–107.
- [33] S. Wang, X. Yang, X. Zhang, X. Ding, Z. Yang, K. Dai, H. Chen, *Appl. Surf. Sci.* 391 (2016) 194–201.
- [34] Y. Zheng, F. Duan, J. Wu, L. Liu, M. Chen, Y. Xie, *J. Mol. Catal. A: Chem.* 303 (2009) 9–14.
- [35] M.C. Payne, M.P. Teter, D.C. Allan, T.A. Arias, J.D. Joannopoulos, *Rev. Mod. Phys.* 64 (1992) 1045.
- [36] J.P. Perdew, K. Burke, M. Emzerhof, *Phys. Rev. Lett.* 77 (18) (1996) 3865.
- [37] D. Vanderbilt, *Phys. Rev. B* 41 (1990) 7892.
- [38] H.J. Honkhorst, J.D. Pack, *Phys. Rev. B* 13 (1976) 5188–5192.
- [39] Z. Wang, C. Yang, T. Lin, H. Yin, P. Chen, D. Wan, F. Xu, F. Huang, J. Lin, X. Xie, M. Jiang, *Adv. Funct. Mater.* 23 (2013) 5444–5450.
- [40] R.M. Moon, T. Riste, W.C. Koehler, S.C. Abrahams, *J. Appl. Phys.* 40 (1969) 1445–1447.
- [41] H. Li, K. Li, H. Wang, *Mater. Chem. Phys.* 116 (2009) 134–142.
- [42] I. Justicia, P. Ordejón, G. Canto, J.L. Mozos, J. Fraxedas, G.A. Battiston, R. Gerbasi, A. Figueras, *Adv. Mater.* 14 (2002) 1399–1402.
- [43] M. Shang, W. Wang, L. Zhang, H. Xu, *Mater. Chem. Phys.* 120 (2010) 155–159.
- [44] K. Lai, W. Wei, Y. Zhu, M. Guo, Y. Dai, B. Huang, *J. Solid State Chem.* 187 (2012) 103–108.
- [45] C. Wan, D.-g. Cheng, F. Chen, X. Zhan, *RSC Adv.* 5 (2015) 42609–42615.
- [46] T. Leshuk, R. Parviz, P. Everett, H. Krishnakumar, R.A. Varin, F. Gu, *ACS Appl. Mater. Interfaces* 5 (2013) 1892–1895.
- [47] K.J. May, C.E. Carlton, K.A. Stoerzinger, M. Risch, J. Suntivich, Y.-L. Lee, A. Grimaud, Y. Shao-Horn, *J. Phys. Chem. Lett.* 3 (2012) 3264–3270.
- [48] S. Bae, S. Kim, S. Lee, W. Choi, *Catal. Today* 224 (2014) 21–28.
- [49] S.-K. Lee, A. Mills, *Chem. Commun.* 18 (2003) 2366–2367.
- [50] Z. Zhao, W. Zhang, Y. Sun, J. Yu, Y. Zhang, H. Wang, F. Dong, Z. Wu, *J. Phys. Chem. C* 120 (2016) 11889–11898.
- [51] Z. Ni, F. Dong, H. Huang, Y. Zhang, *Catal. Sci. Technol.* 6 (2016) 6448–6458.
- [52] A. Janotti, C.G. Van de Walle, *Appl. Phys. Lett.* 87 (2005) 122102.
- [53] M.A. Butler, *J. Appl. Phys.* 48 (1977) 1914–1920.
- [54] H. Huang, Y. He, X. Li, M. Li, C. Zeng, F. Dong, X. Du, T. Zhang, Y. Zhang, *J. Mater. Chem. A* 3 (2015) 24547–24556.
- [55] M. Kong, Y. Li, X. Chen, T. Tian, P. Fang, F. Zheng, X. Zhao, *J. Am. Chem. Soc.* 133 (2011) 16414–16417.
- [56] X. Meng, Z. Zhang, *Appl. Catal. B Environ.* 209 (2017) 383–393.
- [57] Y. Zhang, Y. Zhu, J. Yu, D. Yang, T.W. Ng, P.K. Wong, J.C. Yu, *Nanoscale* 5 (2013) 6307–6310.
- [58] Q.J. Xiang, J.G. Yu, M. Jaroniec, *J. Phys. Chem. C* 115 (2011) 7355–7363.
- [59] H. Huang, S. Wang, N. Tian, Y. Zhang, *RSC Adv.* 4 (2014) 5561–5567.
- [60] D. Wang, H. Shen, L. Guo, C. Wang, F. Fu, Y. Liang, *RSC Adv.* 6 (2016) 71052–71060.
- [61] D. Morales-Cruza, F. Paraguay-Delgado, R. Borja-Urby, S. Basurto-Cereceda, G. Herrera-Perez, P. Longo, M. Malac, *Mater. Sci. Semicond. Process.* 63 (2017) 184–189.
- [62] R.J. Elliott, *Phys. Rev.* 108 (1957) 1384–1389.
- [63] T. Etienne, E. Mosconi, F. De Angelis, *J. Phys. Chem. Lett.* 7 (2016) 1638–1645.
- [64] F. Zheng, L.Z. Tan, S. Liu, A.M. Rappe, *Nano Lett.* 15 (2015) 7794–7800.